

THERMOTROPIC LIQUID CRYSTALLINE POLYMER FIBERS*

M. GREGORY FOREST[†], HONG ZHOU[‡], AND QI WANG[§]

Abstract. Super-strength, lightweight materials used in bullet-proof vests, high-performance cables and tires, and stealth airplanes are built from liquid crystalline polymer (LCP) fibers. The remarkable strength properties are dominated by molecular alignment achieved as a result of the complex interactions at play in fiber processes. The fiber manufacturing process begins with a high temperature liquid phase of rigid rod macromolecules, whose orientation couples to the strong elongational free surface flow. The flow exits at a prescribed radius and velocity (v_0), tapers and cools as it evolves downstream, and solidifies along some free boundary, below which a take-up velocity ($v_1 > v_0$) is imposed at a fixed location. Our goal in this paper is a model for this process which realistically couples the hydrodynamics, the LCP dynamics, and the temperature field, along with the free surface and boundary conditions. Moreover, we aim for a model, by necessity complex, that provides nontrivial fiber process predictions and that admits a linearized stability analysis of steady fiber processes. We first generalize three-dimensional Doi–Edwards averaged kinetic equations to include temperature-dependent material behavior and a coupled energy equation. From this formulation we generalize previous isothermal hydrodynamic, isotropic viscoelastic, and anisotropic viscoelastic models, incorporating temperature-dependent material response. The model, its nontrivial boundary value solutions, and their linearized stability are presented, along with the translation of these mathematical results, to industrially relevant issues of fiber performance properties and bounds on stable spinning speeds.

Key words. fibers, liquid crystalline polymers, modeling

AMS subject classifications. 34, 35, 76

PII. S0036139998336778

1. Introduction. Models for steady fiber spinning (depicted in Figure 1) of *isotropic polymer melts* are well developed, beginning with the work of Matovich and Pearson [30], who introduced a heuristic derivation of isothermal viscous liquid fiber models. Many refinements have followed of both mathematical and physical importance; we note developments for viscous [12, 36] and isotropic viscoelastic [2, 5, 11] constitutive laws and for thermal effects [25, 27, 28, 39, 45], and numerous other references cited therein.

Our interest in this paper is in a model that couples thermal effects and anisotropic viscoelasticity to the standard hydrodynamic thin-filament equations [5, 36]. The solutions we focus on are nontrivial steady states of the two-point boundary value problem for fiber processes, as stated in the abstract. The model consists of a system of cou-

*Received by the editors February 27, 1998; accepted for publication (in revised form) June 15, 1999; published electronically March 23, 2000. This research was sponsored by the Air Force Office of Scientific Research, Air Force Materials Command, USAF under grants F49620-97-1-0001 and F49620-96-1-0131 and by the National Science Foundation under grant DMS 9704549. The US Government is authorized to reproduce and distribute reprints for governmental purposes notwithstanding any copyright notation thereon. The views and conclusions contained herein are those of the authors and should not be interpreted as necessarily representing the official policies or endorsements, either expressed or implied, of the Air Force Office of Scientific Research or the US Government.

<http://www.siam.org/journals/siap/60-4/33677.html>

[†]Department of Mathematics, University of North Carolina, Chapel Hill, NC 27599-3250 (forest@amath.unc.edu).

[‡]Department of Mathematics, University of North Carolina, Chapel Hill, NC 27599-3250 (hongzhou@amath.unc.edu). Current address: Department of Mathematics, University of California at Santa Cruz, Santa Cruz, CA 95064 (hongzhou@math.ucsc.edu).

[§]Department of Mathematical Sciences, Indiana University-Purdue University at Indianapolis, Indianapolis, IN 46202 (wang@bigswr.iupui.edu).

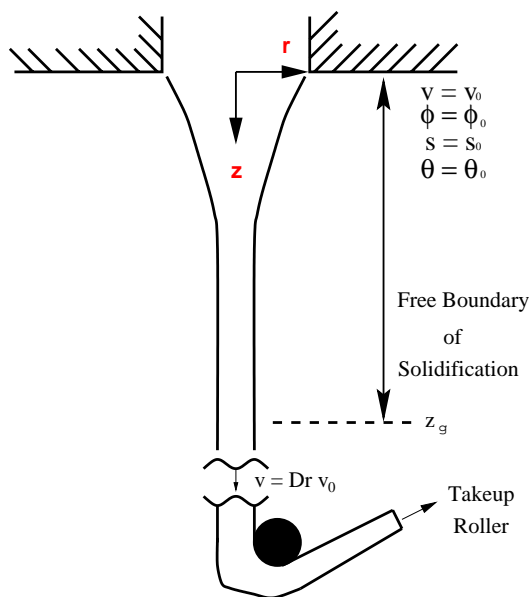


FIG. 1. A schematic diagram of a single fiber in a spinning process.

pled nonlinear PDEs (for the fiber radius, axial fluid velocity, fiber temperature, and an orientation order parameter) in one space dimension (the axis of the filament), with a variety of important material and processing parameters. This complexity is unavoidable if one wants to model actual thermotropic liquid crystalline polymer (TLCP) spinline: the material is viscous, elastic, and anisotropic, and each of these rheological properties varies with temperature. The process couples inertia, gravity, free surface effects, and upstream and downstream boundary conditions. Previous models have isolated limited physical competitions (e.g., thermal viscous fibers [41] or isothermal LCP fibers [20, 21]), but the goal here is to provide a realistic comprehensive model and point out how the complex hydrodynamic, thermal, and anisotropic elastic effects of TLCPs interact in concert. We deduce the leading order balance equations for a slender fiber flow from a nondimensional scaling based on industrially relevant scales for LCPs. The perturbation method follows closely the analysis described in detail in [4, 5, 20] for isothermal axisymmetric fibers. This derivation is a natural next step in the slender, longwave asymptotic analysis of inviscid [38], viscous [12, 24, 36], and isotropic viscoelastic [4, 5] liquid fibers.

In order to model TLCPs, we first have to extend the three-dimensional (3-D) Doi theory [6] to include thermal material dependence. The full slender fiber model then follows in a straightforward, albeit quite tedious, generalization of [20, 21, 34].

We remark that the usefulness and purpose of industrial spin models is threefold: first, to infer spun-fiber performance properties for given material properties and processing conditions; second, as a tool to target performance properties by varying material behavior or the process; and third, to determine bounds on how fast the process can run.

Performance properties (e.g., elastic modulus) are dominated by, and inferred from, the final anisotropic degree of orientation of the spun fiber; the mesoscale mea-

sure of average molecular orientation is the uniaxial nematic order parameter s . This order parameter is directly related to fiber birefringence, Δn , by

$$(1.1) \quad s = \Delta n / \Delta n_{max},$$

where Δn is the experimentally measured birefringence of the LCP melt and Δn_{max} is the maximum birefringence possible for the amorphous LCP melt. It is a remarkable fact that industry spin models since 1969 [30] were developed solely to predict the spun-fiber birefringence, $\Delta n = s \Delta n_{max}$. Yet prior to the coupling of anisotropic constitutive laws [21, 34], the standard practice in industry was to invoke an empirical stress-optical law from rubber network theory to infer birefringence a posteriori, as follows. First a viscous nonisothermal spin model [23] produces axial stress near glass transition, $\tau_{axial}(z_g)$, from which birefringence is inferred:

$$(1.2) \quad \Delta n = C_{opt} \tau_{axial}(z_g) + C_o,$$

where C_{opt} is a stress-optical coefficient (a material property) and C_o is a constant. The anisotropic LCP model of [21, 34] reproduces the empirical stress-optical law (1.2) in the weakly ordered limit, $s \sim 0$, which is applicable to weakly birefringent materials like polyethylene terephthalate (PET). At full capacity, though, i.e., for strongly birefringent materials like LCPs, our model computes the entire nonlinear evolution of birefringence in the spinline, as it interacts with hydro- and thermodynamical effects.

There is a second fundamental advance of the model presented here. The linearized stability of steady thermal fiber processes which undergo liquid to solid phase changes has been prohibited by a peculiar feature of previous models and codes [23, 26]. Namely, the flow was modeled as a two-phase flow. Above glass transition temperature (θ_g) the full hydrodynamic and thermal equations are enforced. For temperature below the glass transition ($\theta < \theta_g$) the fiber is modeled as a rigid solid fiber, i.e., the hydrodynamic equation is simply $v \equiv v_1$. Mathematically, this corresponds to a discontinuous gradient in the system of equations at the free boundary $z = z_g$ where $\theta(z) = \theta_g$. Therefore a linearization of the steady state profile does not yield a well-defined operator on which to compute eigenfunctions and corresponding growth rates. Below we propose a single-phase model (analogous to a phase field model [8, 42]) that removes this arbitrary condition. We show that when the material is accurately characterized, the single- and two-phase models agree—i.e., the liquid fiber smoothly approaches the constant take-up velocity at the free boundary where θ approaches θ_g . We then proceed to implement a linearized stability analysis and code for nontrivial steady TLCP fiber processes. Predictions of the critical take-up speed (so-called draw ratio) are then given as a function of processing conditions.

We remark that in no actual spin process is there any evidence of a discontinuity in velocity gradient at the glass transition free boundary. We therefore assert that a fair benchmark of any thermal fiber model and associated material characterization is the condition that the velocity smoothly approaches the imposed take-up speed as the material reaches glass transition temperature. Such benchmarks were satisfied for our model only after we modified the material parameters provided by colleagues at Hoechst–Celanese Corporation. Figures 2–6 illustrate this point.

We emphasize that this paper represents an intermediate modeling advance by admitting temperature effects only to the extent that one-dimensional (1-D) models and derivations remain self-consistent. As noted by Vassilatos, Schmelzer, and Denn [39] and Wang and Forest [41], the 1-D perturbation theories are based on a slenderness

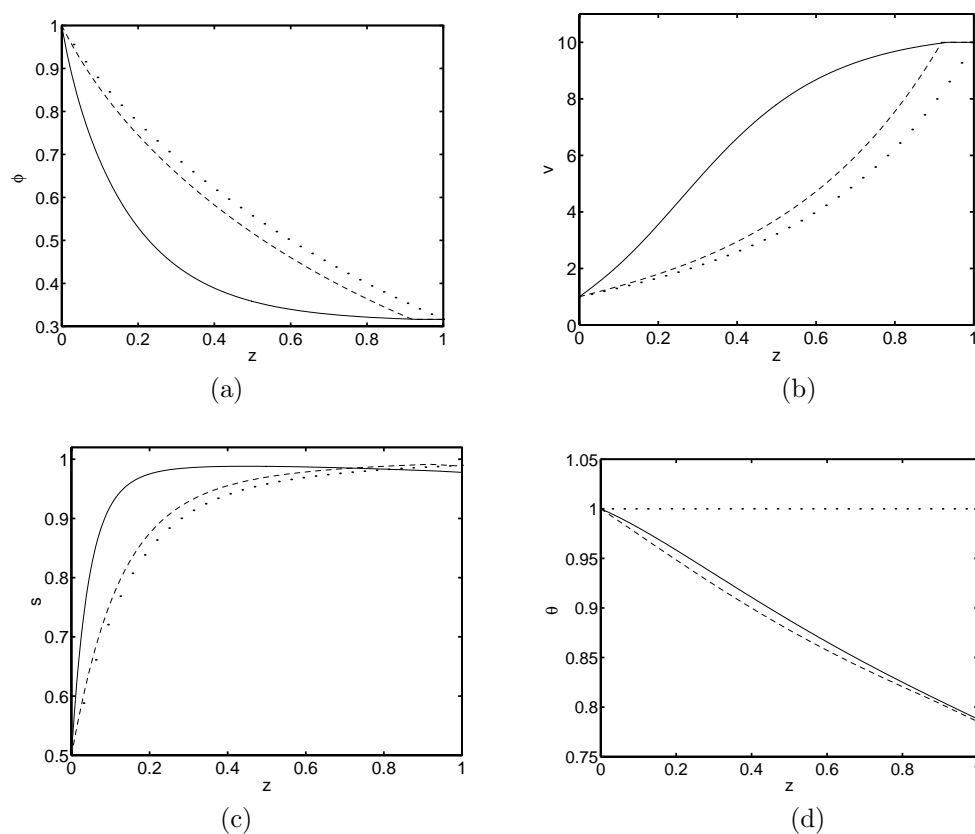


FIG. 2. Typical isothermal (dotted) and nonisothermal (dashed, solid) steady spinning solutions from a two-phase model. All parameter values are fixed at order one values: $\alpha = 5$, $Re = 0.2$, $1/W = 1/F = \Lambda_0 = 1$, $St = \omega = 1$, $N = 4$, $\sigma_d = 0.5$, $\theta_0 = 0.8$, $\mathcal{E} = 1$ (dashed curve), and $\mathcal{E} = 17$ (solid curve). Boundary conditions are $\phi(0) = v(0) = \theta(0) = 1$, $s(0) = 0.5$, $v(1) = 10$. The dotted curves correspond to the isothermal solution, where $\Delta\theta = 0$, $\theta_{ambient} = \theta_{melt}$; the solid and dashed curves correspond to $\Delta\theta = 0.5$, i.e., $\theta_{ambient} = .5\theta_{melt}$.

assumption which requires weak radial dependence in all physical quantities (velocity, pressure, and temperature). The standard perturbation theories break down in the presence of rapid surface cooling, which generates significant radial temperature gradients relative to axial gradients.

As noted in [26, 39, 41], standard 1-D models are necessarily limited to small Biot numbers, i.e., thermal conduction has to dominate surface cooling. These conditions are met in modern spinline within the shrouded part of the spinline, where the temperature is sustained high enough to delay solidification and allow the elongational flow, orientation, and heat conduction to dominate. Models for unshrouded segments of a spinline require either a full two-dimensional (2-D) steady temperature resolution [10, 37, 39, 41, 44] or nonstandard 1-D perturbation theory [26]. For isothermal spinning flows, a full 2-D axisymmetric steady simulation for LCPs was given recently by Mori, Hamaguchi, and Nakamura [32] using the Doi equations [13] in the quadratic closure approximation. To our knowledge, there are no full simulations of free surface TLCPs in spinning flows, so the models and results presented here are the first which

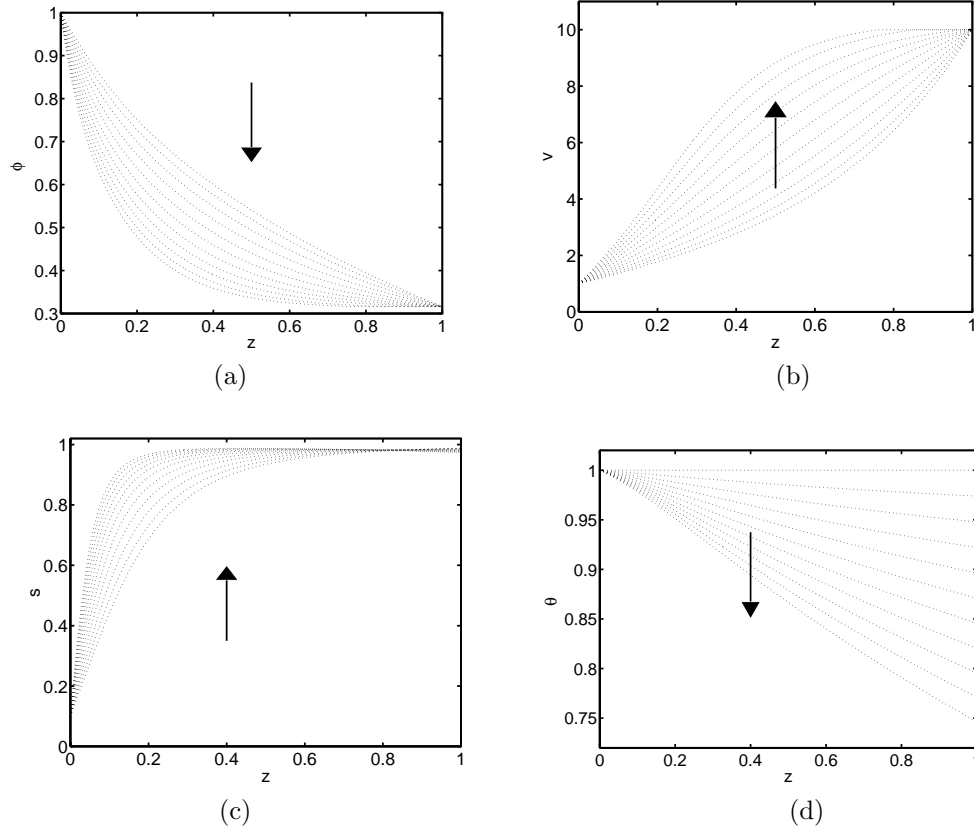


FIG. 3. Steady state variations with respect to the nonisothermal parameter $\Delta\theta$, $0 \leq \Delta\theta \leq 0.6$ in increments of .06; our single-phase model is employed for these figures in increments of .06. All material parameter values and the boundary data ($Dr = 10$) are the same as Figure 2 except that here the initial orientation is prescribed, $s(0) = 0.1$, and the viscosity-temperature Griffith number is prescribed to be a realistic value of $\mathcal{E} = 17$. Arrows indicate the direction of increasing $\Delta\theta$.

resolve a full coupling of hydrodynamics, microstructure, and thermodynamics in a fiber spinning flow.

2. 3-D model formulation. We first provide a temperature-dependent generalization of the 3-D Doi equations for flows of LCPs as given by [6] and [34]. This step in modeling the thermal rheological behavior of TLCPs is nontrivial; we have used the public literature, industry reports, and private consultation with staff rheologists of Hoechst–Celanese Corporation. We note that temperature-dependent density variations of TLCPs are modeled here through the LCP stress and orientation dynamics, but not in mass conservation.

Incompressibility condition.

$$(2.1) \quad \nabla \cdot \mathbf{v} = 0.$$

Conservation of momentum.

$$(2.2) \quad \rho \frac{d}{dt} \mathbf{v} = \nabla \cdot \boldsymbol{\tau} + \rho \mathbf{g},$$

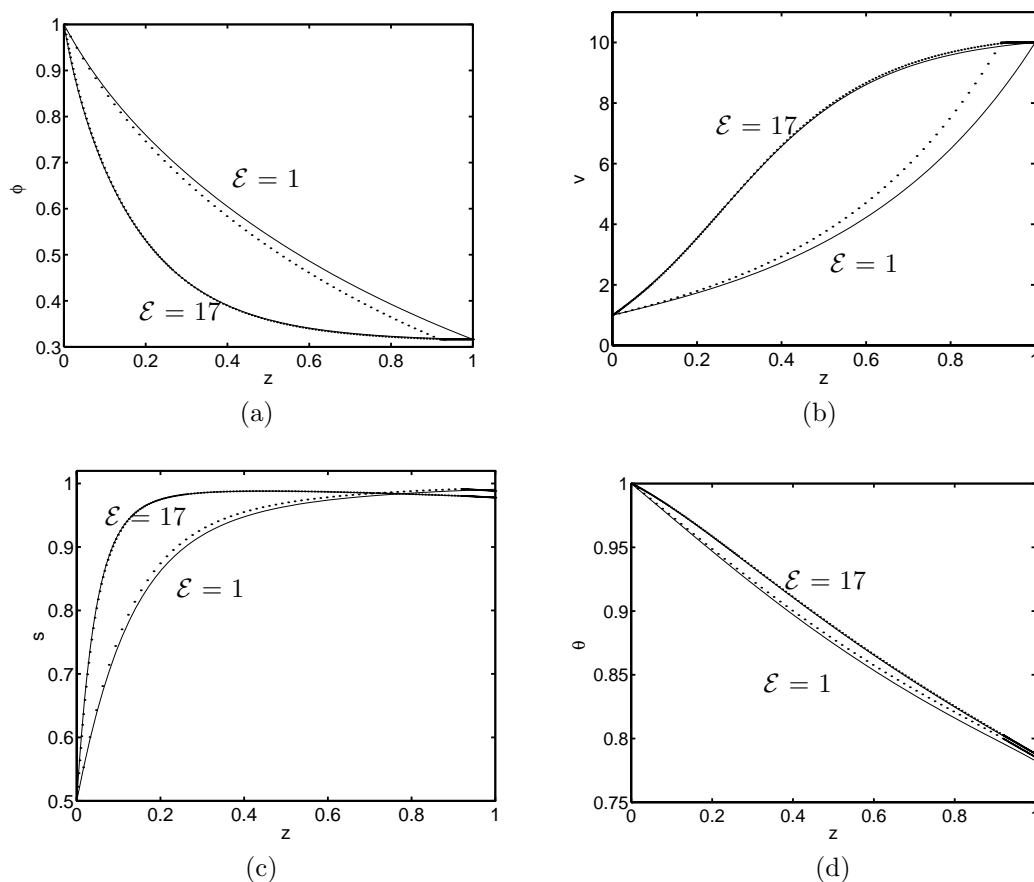


FIG. 4. Comparison of one-phase and two-phase models for different Griffith numbers \mathcal{E} . The dotted lines denote the solutions of the two-phase model, while the solid lines denote the solutions of the one-phase model. All other material parameter values and boundary data are the same as Figure 2.

where ρ is the density of the polymeric liquid, \mathbf{v} is the velocity vector, τ is the total stress tensor, $\rho \mathbf{g}$ is the external force due to gravity, and $\frac{d}{dt}(\cdot)$ denotes the material derivative $\frac{\partial}{\partial t}(\cdot) + \mathbf{v} \cdot \nabla(\cdot)$. Density is assumed constant, so that thermal expansion is presumed a weak effect.

The nematic order is resolved in terms of a second-moment average, $\langle \mathbf{m} \otimes \mathbf{m} \rangle$, of the rigid-rod molecular direction, \mathbf{m} , where the average is with respect to a probability distribution function. The mesoscale orientation tensor is then given by

$$(2.3) \quad \mathbf{Q} = \langle \mathbf{m} \otimes \mathbf{m} \rangle - \frac{1}{3} \mathbf{I},$$

which is a traceless, symmetric second-order tensor. A moment closure rule yields the following flow-orientation coupled system [13, 14, 16, 6], where the molecular orientation induces fluid stresses, and the fluid motion in turn drives the orientation dynamics.

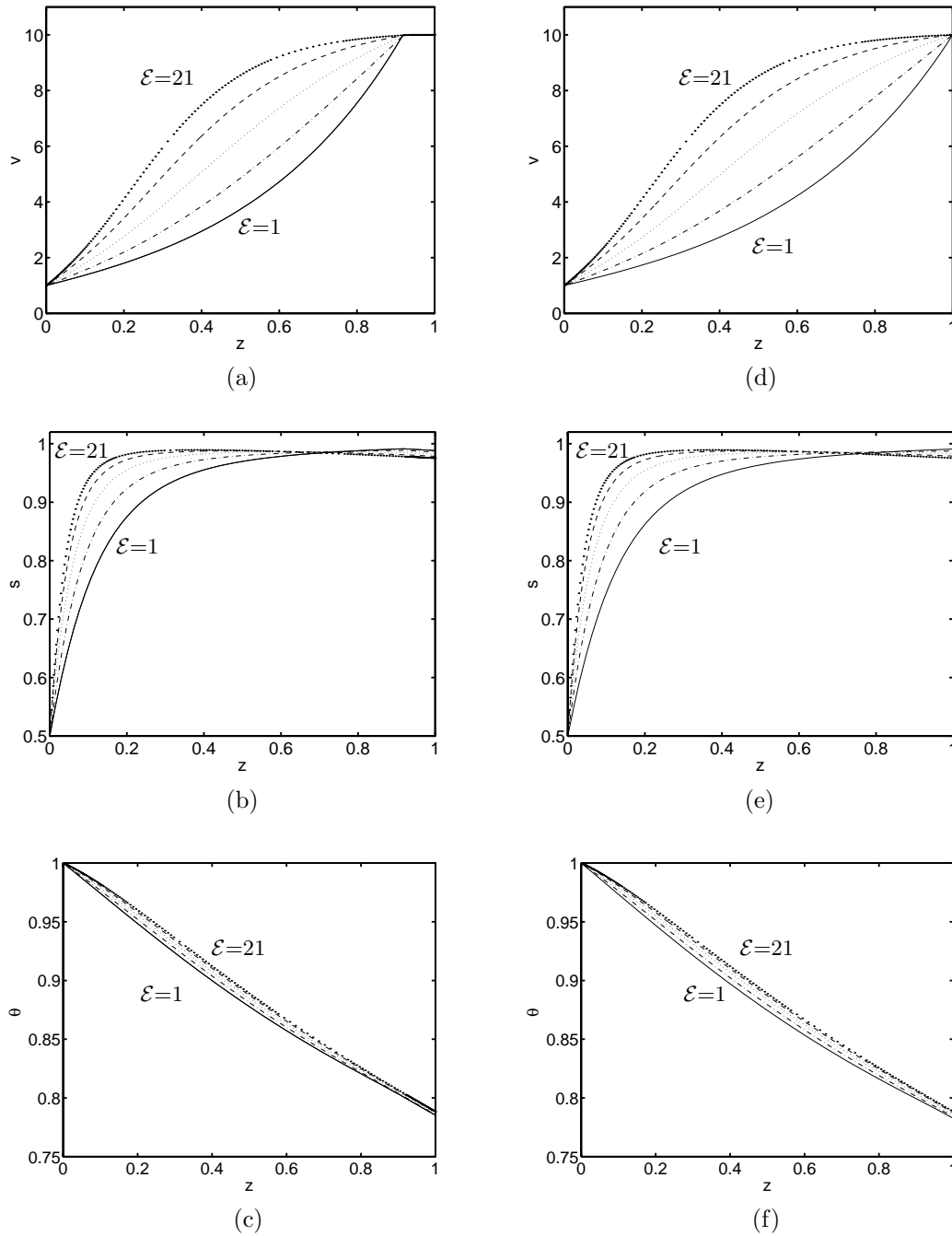


FIG. 5. Change of solution profile due to the change of the activation energy \mathcal{E} , where \mathcal{E} goes from 1 to 21 with an increment of 5. The left column corresponds to the solutions to the standard two-phase model, while the right column provides solutions to the one-phase model. All the other parameters are the same as those in Figure 2.

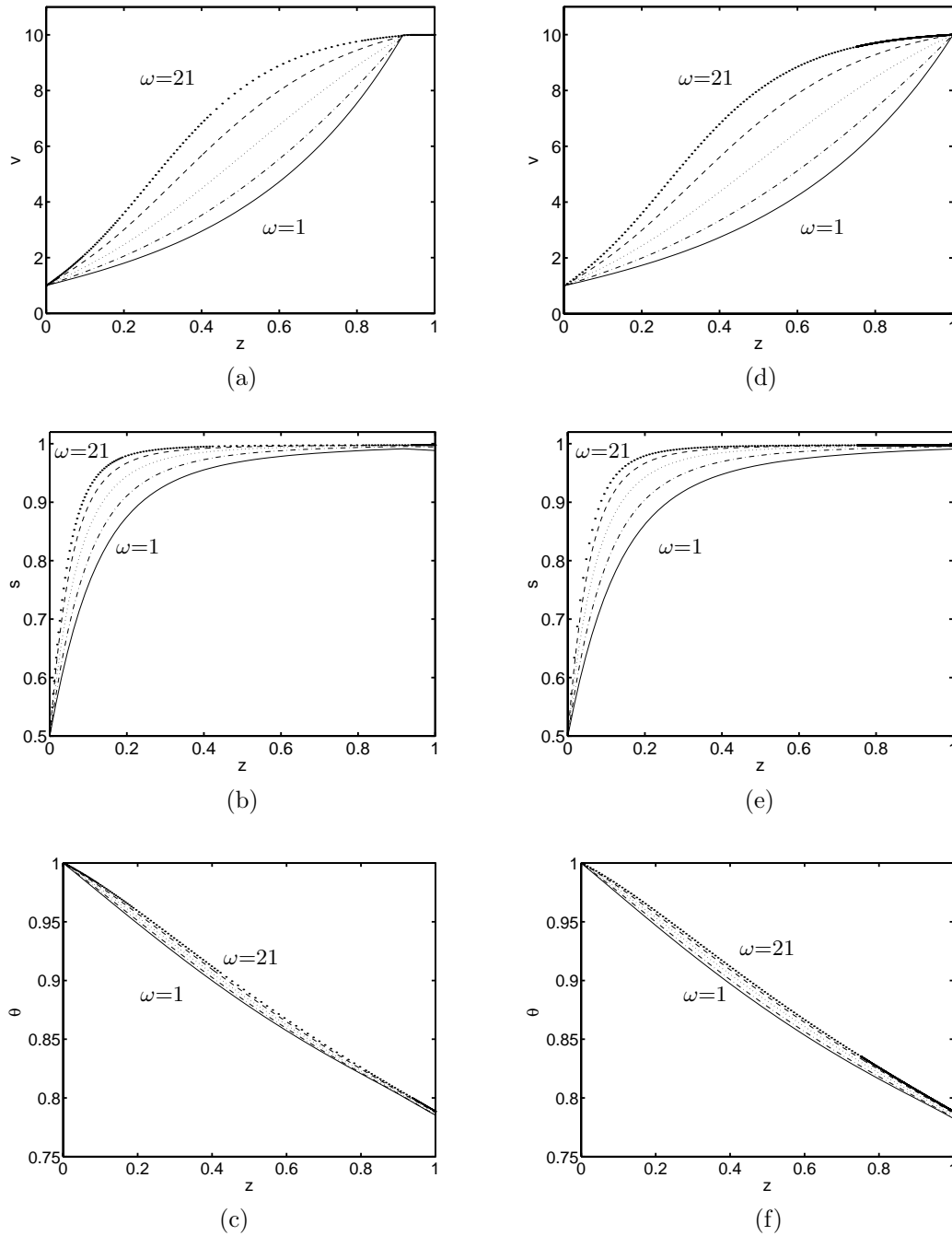


FIG. 6. Change of solution profile due to the change of polymer relaxation thermal rate parameter ω , where ω goes from 1 to 21 with an increment of 5. The left column shows the solutions to the standard two-phase model, the right column solutions to the one-phase model. Here $\mathcal{E}=1$. All the other parameters are the same as those in Figure 2.

Constitutive equation for stresses.

$$\begin{aligned}
 \tau &= -p\mathbf{I} + \hat{\tau}, \\
 \hat{\tau} &= \hat{\tau}_{iso} + \hat{\tau}_{aniso}, \\
 (2.4) \quad \hat{\tau}_{iso} &= 2\eta(\theta)\mathbf{D}, \\
 \hat{\tau}_{aniso} &= 3ck\theta[(1 - N/3)\mathbf{Q} - N(\mathbf{Q} \cdot \mathbf{Q}) + N(\mathbf{Q} : \mathbf{Q})(\mathbf{Q} + \mathbf{I}/3) \\
 &\quad + 2\lambda(\theta)(\nabla\mathbf{v}^T : \mathbf{Q})(\mathbf{Q} + \mathbf{I}/3)],
 \end{aligned}$$

where \mathbf{D} is the rate-of-strain tensor, $\mathbf{D} = \frac{1}{2}(\nabla\mathbf{v} + \nabla\mathbf{v}^t)$, and p is the scalar pressure. In (2.4) $\eta(\theta)$ is modeled as the effective isotropic viscosity, presumed to obey an Arrhenius relation,

$$(2.5) \quad \eta(T) = \eta_0 e^{E/R(1/\theta - 1/\theta_0)},$$

where E is the activation energy, R is the gas constant, and η_0 is the effective isotropic viscosity for LCPs at an experimental temperature θ_0 above the melting point. The term $\hat{\tau}_{aniso}$ in (2.4) corresponds to orientational stress, where c is the number of polymer molecules per unit volume, and $\lambda(\theta)$ is the relaxation time of the LCP molecules associated with rotation of the rigid rod-like molecules. We also posit an Arrhenius relation for relaxation time,

$$(2.6) \quad \lambda(\theta) = \lambda_0 e^{\omega(1/\theta - 1/\theta_0)},$$

where λ_0 is the relaxation time of the LCP at the temperature θ_0 , and ω is a parameter (units of temperature) to be determined from experiments. In addition, N is a dimensionless measure of the LCP density c which characterizes the strength and shape of the short-range intermolecular potential (see Appendix C), k is the Boltzmann constant, and θ is absolute temperature.

Without loss of generality, we select the same experimental temperature θ_0 in (2.5) and (2.6), which we later choose as the melt temperature for convenience, i.e., $\theta_0 = \theta_{melt}$. Any other choice of experimental temperatures amounts to a simple rescaling in which the products $\eta_0 e^{-E/(R\theta_0)}$ and $\lambda_0 e^{-\omega/\theta_0}$ are independent of θ_0 in accordance with these Arrhenius forms.

Orientation tensor equation (anisotropic elastic coupling).

$$(2.7) \quad \left\{ \begin{aligned} &\frac{d}{dt}\mathbf{Q} - (\nabla\mathbf{v}^T \cdot \mathbf{Q} + \mathbf{Q} \cdot \nabla\mathbf{v}) = F(\mathbf{Q}) + G(\mathbf{Q}, \nabla\mathbf{v}), \\ &F(\mathbf{Q}) = -\sigma_d/\lambda(\theta)\{(1 - N/3)\mathbf{Q} - N(\mathbf{Q} \cdot \mathbf{Q}) + N(\mathbf{Q} : \mathbf{Q})(\mathbf{Q} + \mathbf{I}/3)\}, \\ &G(\mathbf{Q}, \nabla\mathbf{v}) = \frac{2}{3}\mathbf{D} - 2(\nabla\mathbf{v}^T : \mathbf{Q})(\mathbf{Q} + \mathbf{I}/3). \end{aligned} \right.$$

Here σ_d is a dimensionless parameter describing the anisotropic drag that a molecule experiences as it moves relative to the solution; $0 \leq \sigma_d \leq 1$, where $\sigma_d = 1$ is the isotropic friction limit and $\sigma_d = 0$ is the highly anisotropic limit. Note that F characterizes the orientation dynamics independent of flow, whereas G describes the flow-orientation interaction.

Energy equation.

$$(2.8) \quad \rho C \frac{d\theta}{dt} = \hat{\tau} : \mathbf{D} - \nabla \cdot \mathbf{q},$$

where C is the specific heat per unit mass and \mathbf{q} is the heat flux vector. The term $\hat{\tau} : \mathbf{D}$ models viscous heating, which is a weak effect but it is included for the sake of completeness.

Heat loss boundary condition.

$$(2.9) \quad \mathbf{q} \cdot \mathbf{n}_f = -h(\theta - \theta_a),$$

where θ_a is the ambient temperature and h is the heat loss coefficient. We use a Fourier law for the heat flux \mathbf{q} ,

$$(2.10) \quad \mathbf{q} = -K\nabla\theta,$$

where K is the thermal conductivity.

Note. Standard two-phase models [23, 26, 41] apply a simplified momentum equation once $\theta \leq \theta_g$. In particular, the velocity is assumed constant in the solid phase:

$$(2.11) \quad \frac{d\mathbf{v}}{dz} = 0.$$

The equations for the orientation tensor and the energy equation still apply. Note that the energy (2.8) decouples when $v = \text{constant}$, so that one may integrate the steady-state temperature exactly. Then the temperature solution yields a variable coefficient, uncoupled orientation (2.7). This structure will be evident in the 1-D model to follow.

Axisymmetric free surface and corresponding boundary conditions. We adopt cylindrical coordinates (r, θ, z) with the axial direction coincident with the direction of gravity, and with orthonormal basis $\mathbf{e}_r, \mathbf{e}_\theta, \mathbf{e}_z$ (Figure 1). The velocity is given by

$$(2.12) \quad \mathbf{v} = (v_r, 0, v_z),$$

where we assume $v_\theta = \mathbf{v} \cdot \mathbf{e}_\theta = 0$. This torsionless assumption is for simplicity and may be generalized to allow for axisymmetric twist in the flow. The axisymmetric free surface is given by

$$(2.13) \quad r = \phi(z, t).$$

The kinematic boundary condition is

$$(2.14) \quad \frac{d}{dt}(r - \phi(z, t)) = 0;$$

i.e., the free surface convects with the flow.

The kinetic boundary conditions are

$$(2.15) \quad (\tau - \tau_a)\mathbf{n}_f = -\sigma_s\kappa\mathbf{n}_f,$$

where \mathbf{n}_f is the unit outward normal of the free surface (2.13), σ_s is the surface tension coefficient, κ is the mean curvature of the free surface given by

$$(2.16) \quad \kappa = \phi^{-1}(1 + \phi_z^2)^{-1/2} - \phi_{zz}(1 + \phi_z^2)^{-3/2},$$

and τ_a is the ambient stress tensor. This condition indicates that the shear stress is continuous across the free surface in the tangential direction whereas the normal stress is discontinuous with jump proportional to surface tension times mean curvature. We assume that the ambient stress τ_a arises only from a constant pressure (p_a) , i.e.,

$$(2.17) \quad \tau_a = -p_a\mathbf{I}.$$

Effects of air drag are neglected, but may be inserted through τ_a .

3. 1-D spin model for TLCP filaments. To nondimensionalize the 3-D model, the following characteristic scales are identified:

$$r_0, z_0, t_0, v_0, \theta_{melt};$$

these are the characteristic transverse and axial length scales, characteristic time and velocity scales, and characteristic temperature (chosen as melt temperature), respectively. Upon nondimensionalizing the full set of 3-D equations in cylindrical coordinates (see [20, 21]), the following collection of dimensionless parameters arises:

$$(3.1) \quad \begin{aligned} \epsilon &= r_0/z_0, & \tilde{\eta}_0 &= 1/Re = \eta_0 t_0 / \rho z_0^2, & 1/W &= \sigma_s / \rho r_0 v_0^2, & 1/F &= g t_0^2 / z_0, \\ N, & & \tilde{\lambda}_0 &= \lambda_0 / t_0, & \tilde{\theta}_g &= \theta_g / \theta_{melt}, & \alpha &= 3ck\theta_{melt} / \rho v_0^2, \\ \sigma_d, & & Pe &= \frac{\rho C z_0^2}{K t_0}, & Br &= \frac{\eta_0 z_0^2}{K \theta_{melt} t_0^2}, & Bi &= \frac{h r_0}{K}, \\ St &= \frac{h z_0}{\rho C v_0 r_0}, & \mathcal{E} &= \frac{E}{R \theta_{melt}}, & \tilde{\omega} &= \omega / \theta_{melt}, & \Delta\theta &= 1 - \theta_a / \theta_{melt}. \end{aligned}$$

Each of these parameters is important and carries physical information about the geometry, the flow, or the material rheology.

- Geometric parameter: ϵ is the aspect ratio of the fiber, the fundamental small parameter upon which slender ($0 < \epsilon \ll 1$) longwave axial equations are deduced from [20]; a typical value is $\epsilon = 0.01$.
- Standard hydrodynamic parameters: Re, W, F are the Reynolds, Weber, and Froude numbers, which respectively parametrize effective isotropic viscosity, surface tension, and gravity, each relative to inertia.
- LCP material parameters: α parametrizes the molecular kinetic energy per unit volume relative to inertial energy per unit volume; from the constitutive law one sees also that α characterizes the molecular stress relative to inertial stress; the combination $\alpha \tilde{\lambda}_0$ characterizes the relaxational stress due to molecular rotation relative to inertial stress; σ_d is the anisotropic drag parameter and $\sigma_d / \tilde{\lambda}_0$ parametrizes anisotropic drag on polymer molecular motion relative to the solvent; N is a polymer density parameter that enters prominently in the intermolecular excluded-volume potential (defined below (3.4), again in Appendix C, then depicted in Figure 12 as a function of N).
- Thermal parameters: Pe is the Peclet number which is a measure of specific heat relative to thermal conductivity; Br is the Brinkman number describing viscous heating relative to thermal conductivity; Bi is the Biot number characterizing the heat loss relative to thermal conductivity; St is the Stanton number, which is the dimensionless heat transfer coefficient, and $Bi = St \cdot Pe \cdot \epsilon^2$; \mathcal{E} is the Griffith number quantifying the degree of viscosity variation with temperature.
- Processing parameter: A nonisothermal parameter $\Delta\theta$ is introduced to measure the degree of nonisothermality. When $\theta_a = \theta_{melt}$, then $\Delta\theta = 0$ and our model reduces to the isothermal case of [21]. We will vary the parameter $\Delta\theta$ to study the energy effects on our previous isothermal LCP spin model predictions [21]. Note that in dimensional units, given $\Delta\theta$, the ambient temperature is $\theta_a \equiv (1 - \Delta\theta) \theta_{melt}$.

The extension of the perturbation formalism of Forest, Wang, and Bechtel [20] to TLCPs is straightforward. The leading order orientation tensor representation is provided in Appendix A, and the corresponding stress tensor components are given in Appendix B. The only new ingredient is the temperature expansion, which is uniform in r and ϵ to leading order. Next we need to pick a physical regime such that these

expansions, when applied to the full 3-D equations, yield consistent 1-D slender fiber equations. The following equations follow when all nondimensional parameters in (3.1) are presumed $\mathcal{O}(1)$ with respect to ϵ except the Biot number which must be $o(1)$ with respect to ϵ , e.g., $Bi \sim \mathcal{O}(\epsilon^2)$. This means we confidently model only weak surface cooling relative to thermal conduction, as mentioned in the introduction.

1-D thermal flow-orientation models for axisymmetric LCP filaments.

We give the minimum set of coupled equations which govern the leading order approximation of each unknown: ϕ , the *free surface radius*; v , the *axial velocity*; u , the *radial velocity*; p , the *pressure*; s , the *uniaxial order parameter*; θ , the *temperature*. (All \sim overbars on nondimensional parameters are dropped from here on.)

LCP melt phase ($\theta \geq \theta_g$).

$$(3.2) \quad \begin{cases} (a) \ (\phi^2)_t + (v\phi^2)_z = 0, \\ (b) \ (\phi^2 v)_t + (\phi^2 v^2)_z = \frac{1}{F}\phi^2 + \frac{1}{W}\phi_z + (\phi^2(R_{eff}^{-1}(s, \theta)v_z + \alpha\theta U(s)))_z, \\ (c) \ s_t + vs_z = v_z(1-s)(2s+1) - \frac{\sigma_d}{\Lambda(\theta)}U(s), \\ (d) \ u = -v_z/2, \\ (e) \ p = \frac{1}{W}\phi^{-1} - e^{\mathcal{E}(1/\theta-1)}v_z/Re - \frac{1}{3}\alpha\theta U(s) + \frac{2}{3}\alpha\Lambda(\theta)\theta s(1-s)v_z, \\ (f) \ \theta_t + v\theta_z = \frac{1}{Pe}\phi^{-2}(\phi^2\theta_z)_z - 2St\phi^{-1}(\theta - 1 + \Delta\theta) + \frac{Br}{Pe}(R_{eff}^{-1}(s, \theta)v_z + \alpha\theta U(s))v_z, \end{cases}$$

where $\Lambda(\theta)$ is the scaled LCP relaxation time

$$(3.3) \quad \Lambda(\theta) = \Lambda_0 e^{\omega(1/\theta-1)};$$

$R_{eff}(s, \theta)$ is an effective 1-D flow-orientation Reynolds number,

$$(3.4) \quad R_{eff}^{-1}(s, \theta) = 3e^{\mathcal{E}(1/\theta-1)}/Re + 2\alpha\theta\Lambda(\theta)s^2,$$

consisting of a Newtonian contribution $(3e^{\mathcal{E}(1/\theta-1)}/Re)$ and an orientation contribution $(2\alpha\theta\Lambda(\theta)s^2)$; and $U(s) = s(1 - N/3(1-s)(2s+1))$ defines the uniaxial bulk free energy, $\int U(s)ds$. The terms proportional to N arise from the Maier-Saupe intermolecular potential. For isothermal flows absent of gravity ($1/F = 0$), the zeroes of U correspond to order parameter equilibria associated with constant cylindrical LCP filaments, the stability of which are characterized in [20, 19] for various regimes; in the gravity-driven flows considered in this paper there are no constant equilibria.

LCP quasi-solid phase ($\theta < \theta_g$) of standard two-phase models.

$$(3.5) \quad \begin{cases} (a) \ v_z = 0, \\ (b) \ s_t + vs_z = -\frac{\sigma_d}{\Lambda(\theta)}U(s), \\ (c) \ u = 0, \\ (d) \ \phi_z = 0, \\ (e) \ p = -\frac{1}{3}\alpha\theta U(s), \\ (f) \ \theta_t + v\theta_z = \frac{1}{Pe}\theta_{zz} - 2St\phi^{-1}(\theta - 1 + \Delta\theta). \end{cases}$$

Remarks on the quasi-solid phase model. Since $v \equiv \text{constant}$ for $\theta < \theta_g$, and $v(1)$ is prescribed, $v(\theta_g)$ must equal $v(1)$. Given $v \equiv v(1)$ in this phase, the temperature equation (3.5_f) can be integrated exactly, subject to boundary conditions. Next, given $\theta(z)$ for $z_g \leq z \leq 1$, the steady state orientation equation (3.5_b) likewise can

be integrated in explicit quadrature form. Moreover, the behavior of s in the quasi-solid phase is immediately deduced from this simple ODE, completely determined by $\text{sgn}(U(s))$. Thus, one needs only to observe $U(s(z_g))$ to infer the orientation behavior after glass transition. Since the definition of surface tension in the quasi-solid state is not clear, we further drop the term $(W\phi)^{-1}$ in the pressure expression (3.5_e) which corresponds to a purely orientation-induced stress contribution.

The traditional *two-phase model* for nonisothermal spinning applies the melt phase equations (3.2) for $\theta \geq \theta_g$ and the rigid fiber equations (3.5) for $\theta < \theta_g$. The new *one-phase model* applies the melt phase equations (3.2) unconditionally.

A salient feature of the LCP melt phase is that the order parameter s and temperature θ couple to the axial velocity v and filament radius ϕ to form a system of four coupled nonlinear PDEs. These are the slender longwave equations for TLCP fibers; they reproduce previous models [7, 12, 25, 30, 34, 36, 38] in the appropriate physical limits.

Another physical quantity of interest is the axial stress τ_{axial} which is given by

$$(3.6) \quad \tau_{axial} = \hat{\tau}_{zz} - p.$$

From (3.2_e), (3.5_e), and Appendix C, the axial stress τ_{axial} is

$$(3.7) \quad \text{Melt phase } (\theta \geq \theta_g) \quad \tau_{axial} = R_{eff}^{-1}(s, \theta) v_z + \alpha \theta U(s) - \frac{1}{W\phi},$$

$$(3.8) \quad \text{Quasi-solid phase } (\theta \leq \theta_g) \quad \tau_{axial} = \tau_{axial}(z_g) + \alpha [\theta(z) U(s(z)) - \theta(z_g) U(s(z_g))],$$

where z_g is the free-boundary location where glass transition occurs,

$$(3.9) \quad z_g = \{z | \theta(z) = \theta_g; \theta(z) > \theta(z_g) \quad \forall z < z_g\}.$$

Equation (3.7) is an *LCP stress-optical relation*. In the left-hand side of expression (3.8), the first term $\tau_{axial}(z_g)$ corresponds to the locked-in stress at solidification, whereas the second term $\alpha[\theta(z) U(s(z)) - \theta(z_g) U(s(z_g))]$ represents small orientational stress relaxation due to cooling and slight changes in the orientation order parameter. There is experimental evidence from NMR studies of heat-treated spun fibers for some weak reordering of the molecular structure [43]. Some processes prevent such annealing behavior by immersing the fiber in a water bath.

The stress-optical relation (3.7) yields a fundamental relation between the axial fiber stress and the “optical” quantity s . For a uniaxial nematic, the order parameter s is the normalized birefringence, (1.1).

Our model therefore calculates birefringence all along the spinline as it couples to the thermal hydrodynamics of fiber spinning. This model forms the foundation for a prediction of spun fiber performance properties as a function of material and processing parameters. In an industrial code, one couples empirical correlations for air drag and heat loss, together with detailed “in-house” material characterization. Those details are not relevant for our purposes here and are deferred to an engineering study of this model [22].

4. Steady state solutions. Steady states for fiber processes satisfy a two-point boundary value problem; refer to Figure 1. We remark that our model is well-posed with the actual imposed spinline conditions. Consistent with our earlier nondimensionalization, fixed upstream conditions are placed on fiber radius, velocity, and temperature:

$$(4.1) \quad \phi(0) = 1, \quad v(0) = 1, \quad \theta(0) = 1.$$

Two additional boundary conditions are free processing parameters to be specified/ varied in the simulations below:

$$(4.2) \quad s(0), \quad v(1).$$

The upstream degree of orientation ($s(0)$) is a function of spinneret design, whereas the take-up speed ($v(1) = \text{draw ratio} = Dr$) is a measure of process speed and throughput.

Depending on the physical regime, one may need another downstream temperature-related condition:

- If $Pe^{-1} \sim O(1)$ with respect to the slenderness parameter ε , then we require another boundary condition at $z = 1$, which is selected by the assumption that axial thermal conduction is negligible downstream, i.e.,

$$(4.3) \quad \frac{\partial(\phi^2 \theta_z)}{\partial z}(1) = 0.$$

- If $Pe^{-1} \sim o(1)$ with respect to ε , then the temperature equation is reduced to first-order and no boundary condition on $\theta(1)$ is allowed.

The boundary condition (4.3) yields a smooth transition in boundary-value-problem solutions between these two physical regimes. To solve the steady state boundary value problem (3.2), (4.1)–(4.3), we use the public domain code TWPBVP generated by Cash and Wright [9], which is based on implicit Runge–Kutta formulas and adaptive mesh refinement.

4.1. Typical steady state solutions: Influence of thermal effects. We begin with typical steady state solutions, first comparing isothermal and nonisothermal *two-phase* model behavior (Figure 2); two selected thermal states are given (our single-phase model is implemented below). The parameters are chosen to illustrate distinct model behavior, *not* to model any specific physical process. From Figure 2 we make the following observations. Note the isothermal solution is identical with Figure 1 in [21].

- A liquid-to-solid phase transition occurs in both thermal spinning states where the nonisothermal parameter is set to $\Delta\theta = 0.5$, which is typical of spinning processes. Two different Griffith numbers are chosen, $\mathcal{E} = 1$ and $\mathcal{E} = 17$. Thus, for both material-dependent viscosity functions, the fiber cools below glass transition temperature within the spinline.
- Note the nonisothermal, low Griffith number ($\mathcal{E} = 1$) dashed curves indicate a discontinuity in the velocity gradient and fiber slope at the glass transition location. The high Griffith number ($\mathcal{E} = 17$) solid curves lessen the jump in gradients, but the two-phase model equations force this unphysical transition.
- The orientation order parameter s in the thermal case develops more rapidly during the melt phase and significantly more rapidly at physically relevant large Griffith numbers, then levels off as glass transition is approached. The degree of orientation (s) slightly decays after the glass transition in the thermal flow. The spinning flow yields higher orientation than is possible in equilibrium, so while the rigid fiber cools, there is some orientation relaxation back toward the flow-independent equilibrium. This observation is consistent with experimental observation on heat-treated annealing of spun TLCP fibers [46].

Figure 3 displays the dependence of the typical steady state with respect to the nonisothermal parameter $\Delta\theta$, which we vary from 0.0 to 0.6; our single-phase model is

employed. The one-phase and two-phase models yield nearly identical qualitative behavior in this parameter regime, which retains the more physical Griffith number $\mathcal{E} = 17$, but discontinuous gradients persist at glass transition location in the two-phase model solutions. The free surface radius ϕ , the axial velocity v , and the orientation order parameter s exhibit thermal sensitivity to $\Delta\theta$. The salient feature of Figure 3 is

- there is a dramatic change in concavity of the velocity profile as $\Delta\theta$ increases from 0 to 0.6, in response to the thermal coupling.

As $\Delta\theta$ increases (i.e., the ambient becomes cooler), the effective viscosity gets larger (a viscous hardening effect) which we show (Appendix D) is responsible for the change of concavity in the velocity profile.

4.2. Comparison of two-phase and one-phase models. In Figure 4 we compare the thermal solutions of the standard two-phase model and our one-phase model where $\Delta\theta = 0.5$. As evident from Figure 4,

- the discrepancy between the two models is measurable for small Griffith numbers and becomes less significant for large Griffith numbers. The one-phase model removes the unphysical discontinuity in velocity gradient and fiber slope.

Figures 5 and 6 further compare the thermal solutions of the two models by varying the Griffith number \mathcal{E} and polymer relaxation thermal rate parameter ω , respectively.

- As either \mathcal{E} or ω increases, the velocity profile undergoes a change in concavity.
- Again, for large \mathcal{E} or ω , the two models are qualitatively consistent.

In Appendix D we give a detailed explanation of this velocity-shape phenomenon, which is observed in all melt spinning processes and is *not captured by isothermal models*. This phenomenon is analogous to the experimental observations by Burgman [7] where the shape of the upper glass jet changes from a concave jet shape to the expanded jet shape. However, his result is for the jet profile near the upper boundary, while our result is for the jet velocity downstream of the spinneret. One can see from our analysis that there is a critical Griffith number or relaxation thermal rate parameter above which the concavity of the velocity profile switches. This amplifies the importance of accurate material characterization, where we note that $\mathcal{E} \sim 17$ is appropriate for the thermotropic LCP Vectra produced by the Hoechst–Celanese Corporation [43].

Figures 4, 5, and 6 compel us to employ the one-phase model rather than the standard industrial two-phase model [23]. The one-phase model has the *critical advantage* that solutions have continuous gradients at the glass transition free boundary, which not only is consistent with experiments but further enables one to perform a linearized stability analysis of these steady boundary value states. From now on, we restrict ourselves to the one-phase model.

4.3. Thermal effects on spun-fiber birefringence. Recall from formula (1.1) that the downstream degree of orientation, $s(1)$, yields a prediction of the spun-fiber birefringence: $\Delta n = \Delta n_{max} \cdot s(1)$. This fiber property is fundamental to fiber producers; it forms the basis for empirical predictions of fiber performance, such as elongation-to-break and elastic modulus [33].

Figure 7 summarizes the single characteristic, spun-fiber orientation $s(1)$, or equivalently the spun-fiber birefringence $\Delta n = \Delta n_{max} \cdot s(1)$, for a two-parameter family of steady state solutions. We vary the nonisothermal parameter, $\Delta\theta$, and the spinning speed or draw ratio, Dr . The following features are noteworthy.

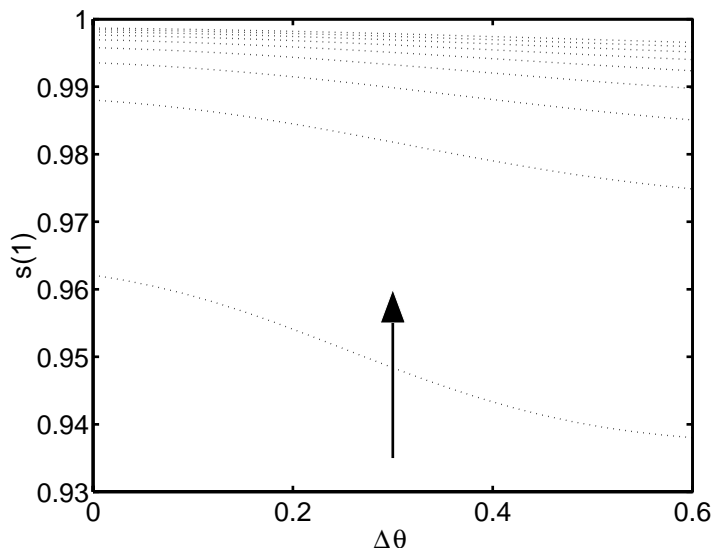


FIG. 7. Thermal response in the spun-fiber orientation, $s(1) = \Delta n / \Delta n_{max}$, due to changes in the nonisothermal parameter $\Delta\theta$ for a wide range of draw ratio Dr . Here $\mathcal{E} = 17$, $\omega = 1$. All the other parameters are the same as in Figure 3. The draw ratio Dr varies from 5 (lower curve) to 45 (top curve) in increments of 5. The arrow indicates the direction of increased Dr .

- For each fixed draw ratio, the spun-fiber orientation drops in response to a cooler ambient temperature ($\Delta\theta$ larger).
- For fixed ambient temperature (i.e., fixed $\Delta\theta$), the spun-fiber orientation increases with higher speed spinning (larger Dr).
- The order of both effects is reduced at higher spinning speeds, *but* it is well known that TLCPs cannot be spun at high speeds because of crystallization effects [17, 29, 31] so the range of Dr from 5 to 15 is most relevant to existing processes. We will revisit the limit on Dr in the stability analysis of section 5.

4.4. Scaling behavior of the glass transition location with the thermal parameter $\Delta\theta$ and draw ratio Dr . Figure 8(a) indicates the effect of ambient temperature on the glass transition location z_g as defined in (3.9) for four selected draw ratios, $Dr = 5, 10, 20$, and 30 , respectively. These figures arise by first computing a two-parameter $(Dr, \Delta\theta)$ family of boundary value solutions, then extracting the spinline location, z_g , of the free boundary of glass transition for each steady state. To better illustrate the effect of ambient temperature, here we pick the Stanton number $St = 2.0$ and all the other parameters are the same as in Figure 3. Recall $\theta_a = \theta_{melt}(1 - \Delta\theta)$. Figure 8(a) conveys

- the critical value of $\Delta\theta$, above or equal to which there is a phase transition, is about 0.276 for $Dr = 5$, 0.312 for $Dr = 10$, 0.360 for $Dr = 20$, 0.384 for $Dr = 30$. For example, at a draw ratio of 10, the ambient temperature must be $.688\theta_{melt}$ or lower for the fiber to solidify within the spinline.
- for fixed draw ratio, the phase transition point z_g moves significantly upstream as the ambient temperature is lowered. For instance, when Dr is fixed to be 10, $z_g = 0.97$ for $\Delta\theta = 0.312$, $z_g = 0.6957$ for $\Delta\theta = 0.396$, $z_g = 0.45$ for $\Delta\theta = 0.576$.

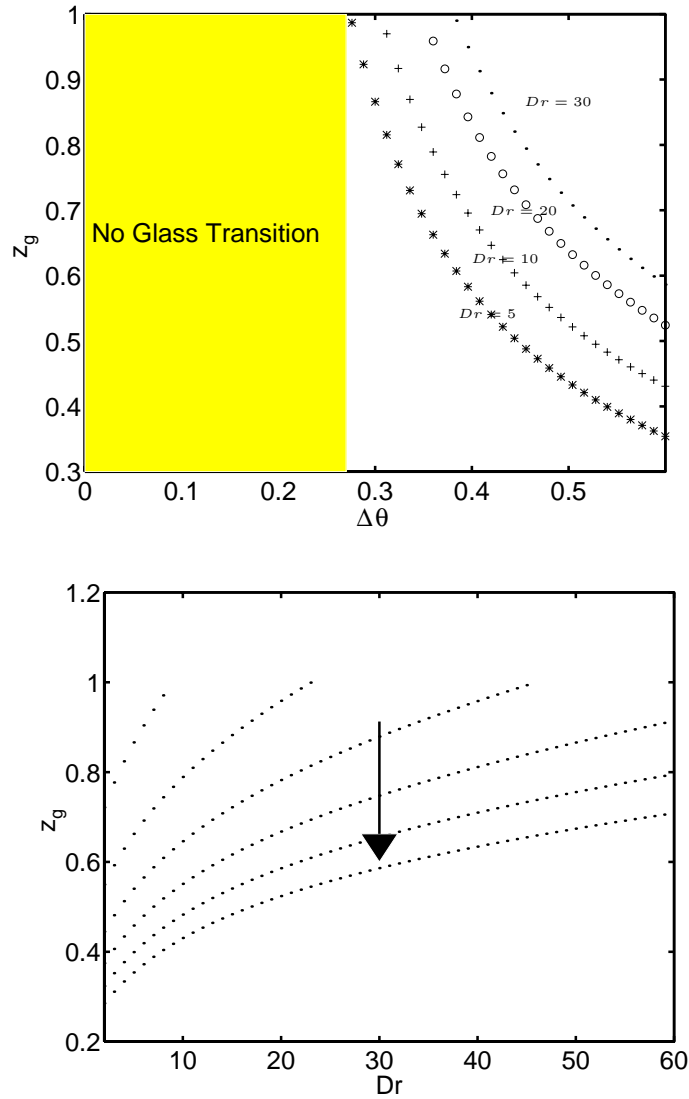


FIG. 8. (a) Glass transition location z_g as a function of the nonisothermal parameter $\Delta\theta$. (b) Variations of z_g as a function of Dr due to changes in $\Delta\theta$: $.3 \leq \Delta\theta \leq .6$ in increments of .06, with the arrow indicating the direction of increasing $\Delta\theta$.

- for fixed ambient temperature, reading vertically in Figure 8(a) confirms the downstream movement of glass transition as the process speeds up (higher Dr).

In Figure 8(b), z_g is plotted as a function of draw ratio Dr corresponding to different values of $\Delta\theta$. When $\Delta\theta$ is smaller than 0.3, there is no liquid-solid phase transition for all Dr varying from 5 to 60. When $\Delta\theta$ is increased to 0.3, spinline glass transition occurs for all Dr between 5 and 10. As $\Delta\theta$ increases, the range of Dr widens for which glass transition takes place. By $\Delta\theta = 0.6$, all Dr up to 60 experience

spinline glass transition.

Figure 8(a) might be used as follows. Suppose a spinline is designed so that glass transition occurs near $z_g = 0.8$, or eight-tenths of the spinline length. Draw a horizontal line at $z_g = 0.8$ in Figure 8(a) and one can easily find the ambient temperature versus draw speed so that $z_g = 0.8$; e.g., for $Dr = 5$, $\Delta\theta = 0.316$ corresponding to $\theta_{ambient} = 68.4\% \theta_{melt}$; for $Dr = 10$, $\Delta\theta = 0.355$ corresponding to $\theta_{ambient} = 64.5\% \theta_{melt}$; for $Dr = 20$, $\Delta\theta = 0.413$ corresponding to $\theta_{ambient} = 58.7\% \theta_{melt}$; for $Dr = 30$, $\Delta\theta = 0.453$ corresponding to $\theta_{ambient} = 54.7\% \theta_{melt}$.

Figure 8(b) provides a wider range of information. For example, $z_g = 0.8$ is achieved for $(Dr = 3.5, \theta_{ambient} = 70\% \theta_{melt})$, $(Dr = 10.5, \theta_{ambient} = 64\% \theta_{melt})$, $(Dr = 38, \theta_{ambient} = 52\% \theta_{melt})$.

In fiber spinning, it is usually desirable to know the location, z^* , where a particular process reaches a preset target property. This information might then, for example, be used to ensure that the target fiber property is reached prior to glass transition. In Figure 9 we select the targeted fiber property to be the degree of LCP orientation, $s = \Delta n / \Delta n_{max}$. We choose several target values of $s = 0.7, 0.8, 0.9$, and 0.95 that the spun fiber must satisfy. We calculate the critical location, z^* , where $s(z^*) = 0.7, 0.8, 0.9$, and 0.95 , respectively, for the starting value $s(0) = 0.1$. Figure 9(a) shows how the location z^* varies due to variations in $\Delta\theta$ for different targeted properties. Figure 9(b) shows the change of the location $z^*(\Delta\theta)$, where $s(z^*) = 0.9$, due to the change of the draw ratio. Figure 9(c) shows the movement in z^* with spinning speed (Dr) for selected ambient cooling conditions ($\Delta\theta$). These figures allow one to explore how the location of desired spun fiber birefringence varies with ambient temperature and draw ratio.

4.5. Thermal effects on axial force at glass transition and at take-up.

Recall (3.7), (3.8) which describe the stress-optical relations for LCP fibers in the melt and quasi-solid phases. We now focus on the *axial force* in the fiber, F_{axial} ,

$$(4.4) \quad F_{axial} = \phi^2 \tau_{axial},$$

at the glass transition (if it occurs) and at the take-up location (we report predictions of axial force rather than stress because that is what can be measured online; see [35]). Figure 10(a) shows thermal influence on fiber axial force at the glass transition location z_g and at the take-up location $z = 1$ for $Dr = 5, 10, 20, 30$, respectively. Figure 10 shows how the axial force at take-up varies with draw ratio and the ambient temperature.

5. Linearized stability. In this section we consider dynamical issues, namely the stability of the nontrivial fiber steady states described above. As discussed in the introduction, our single-phase model allows the numerical bound on stable spinning speed with all other conditions fixed. The stability analysis consists first of (numerically) finding eigenvalues ω_j and corresponding eigenfunctions $\mathbf{f}_j(z)$, $j = 1, 2, \dots$ of the linearization of (3.2) about a given boundary value solution $(\phi, v, s, \theta)(z)$. Linearized solutions take the form $\mathbf{u} = e^{i\omega_j t} \mathbf{f}_j(z)$, so that the real parts of the eigenvalues ω_j , denoted ν_j , are the linearized growth rates. Let

$$(5.1) \quad \nu_{max} = \max_{j \geq 1} \{\nu_j\}.$$

One deduces linearized stability of the steady state $(\phi, v, s, \theta)(z)$ if $\nu_{max} < 0$, linearized instability if $\nu_{max} > 0$, and neutral stability if $\nu_{max} = 0$. The stability or instability of any given steady state is completely characterized by the single diagnostic ν_{max} . The

critical draw ratio Dr^* is thereby defined as the draw ratio at which $\nu_{\max} = 0$. In other words, the critical draw ratio is the critical spinning speed above which a given steady state solution is linearly unstable and below which it is linearly stable. (There is no a priori reason that ν_{\max} does not oscillate about 0; we have not observed this behavior in these calculations, however.)

For isothermal LCPs, Forest, Wang, and Bechtel [21] have already studied linearized stability and how material parameters and processing parameters affect the critical draw ratio. Here we *devote our attention to thermal effects on critical draw ratio*.

To do so, we first formulate linearized stability analysis as an eigenvalue problem as indicated above. Then we solve the eigenvalue problem numerically and use a shooting method to compute the critical draw ratio. We have used 50 and 100 spatial grid points in each computation and then applied a second order extrapolation to achieve higher order accuracy for the critical draw ratio. This analysis extends the work of Burgman [7] and Geyling and Homsy [24] to more complex constitutive behavior.

Figure 11 depicts the critical draw ratio Dr^* as a function of the nonisothermal parameter $\Delta\theta$. As shown in Figure 11, the critical draw ratio grows with $\Delta\theta$. As $\Delta\theta$ increases from 0 to 0.4, Dr^* increases from 37.2 to 269.8. These predictions clearly indicate that

- cooling increases stable spinning speeds for these parameter regimes.

The unusually high critical draw ratio is specific to this parameter regime, which is not relevant to a specific material.

6. Conclusion. We have incorporated temperature-dependent material behavior and an energy equation into the 3-D LCP governing equations of Bhave et al. [6]. From this thermotropic LCP 3-D formulation, we have derived a 1-D thermal thin-filament model for LCPs and proposed a new single-phase model all the way through glass transition. Thermal effects on steady spinning solutions, the downstream orientation order parameter (i.e., spun-fiber birefringence), the glass transition location, and the axial force are deduced. These predictions are fundamental to fiber performance properties. Furthermore, bounds on stable spinning speeds have been generalized from the isothermal studies in [21].

The goals met in this paper are

- the construction of a sophisticated mathematical model, derived from 3-D balances of mass, momentum, energy, and free surface conditions, which resolves the coupling of hydrodynamics, a free surface, microstructural dynamics of LCPs, and thermodynamics;

and

- the application of this model as a tool to explore how material and process conditions influence performance properties and bounds on how fast processes may be run.

The transfer of such a model to an industrial application requires yet another layer of development. For example, the fiber features of interest to experimentalists or industrial practitioners do not consist of the straightforward numerical solution of a two-point boundary value problem. Rather, one must pursue a relationship between solid fiber performance properties (such as tenacity, modulus, and elongation-to-break) and the scientific model prediction of birefringence and axial force at solidification. Today, empirical relations are employed, though clearly there is a need for improvement.

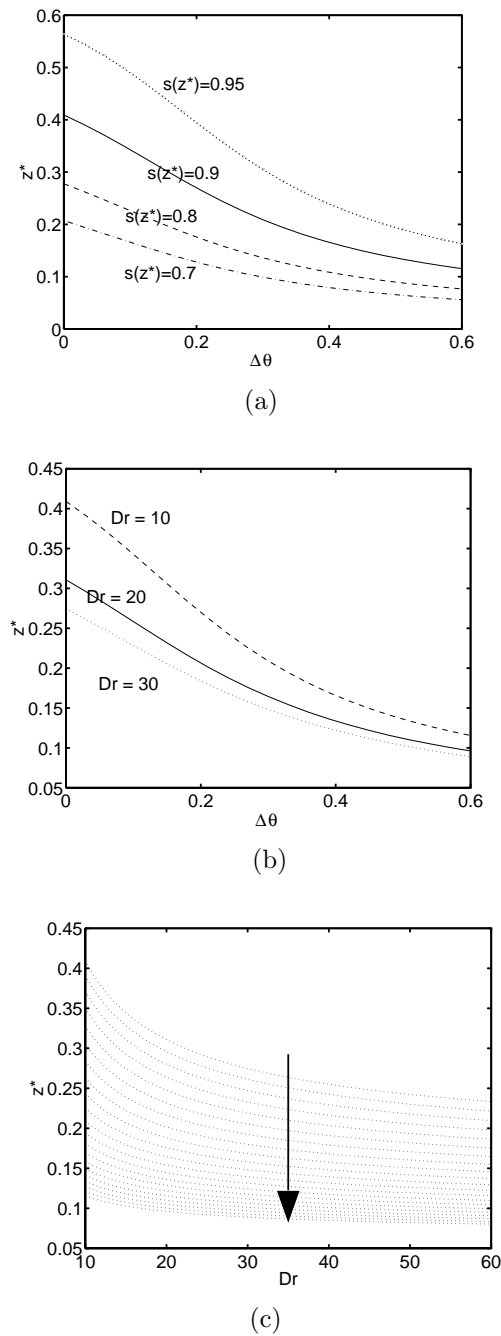


FIG. 9. The spinline location z^* where a target degree of orientation is achieved, as a function of the nonisothermal parameter $\Delta\theta$: (a) $s(z^*; \Delta\theta) = 0.7, 0.8, 0.9, 0.95$, respectively, with the downstream draw ratio $v(1) = 10$. (b) The downstream draw ratio has the values $Dr = 10, 20, 30$, respectively, while the target orientation is fixed at $s(z^*) = 0.9$. (c) Variations of z^* where $s(z^*) = 0.9$ as a function of Dr due to changes in $\Delta\theta$: $0 \leq \Delta\theta \leq 0.6$ in increments of 0.03. The arrow points in the direction of increasing $\Delta\theta$. The upstream degree of orientation is fixed at $s(0) = 0.1$ throughout.

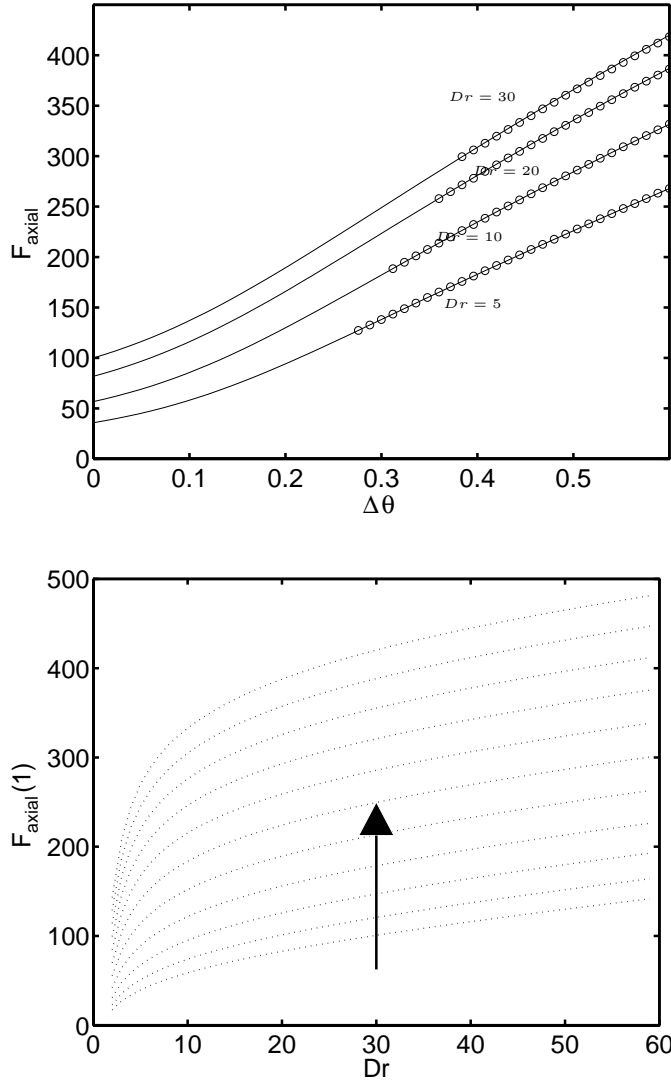


FIG. 10. (a) Axial force F_{axial} evaluated at $z = 1$ (solid curve) and at $z = z_g$ (circle) as a function of $\Delta\theta$ for selected values of draw ratio. (b) Variations of $F_{axial}(1)$ as a function of draw ratio Dr due to changes in $\Delta\theta$, $0 \leq \Delta\theta \leq 0.6$. The arrow indicates the direction of increasing $\Delta\theta$, starting with the isothermal case. All the parameters are the same as in Figure 8.

This requirement in itself presents a major challenge to connect in a fundamental scientific way how mechanical properties transfer during phase transitions.

Appendix A. Orientation representation. In this paper we consider only uniform orientation behavior. At this order of resolution, the orientation tensor \mathbf{Q} is given by [13, 14, 16]

$$(6.1) \quad \mathbf{Q} = s(\mathbf{n}_3 \otimes \mathbf{n}_3 - \mathbf{I}/3),$$

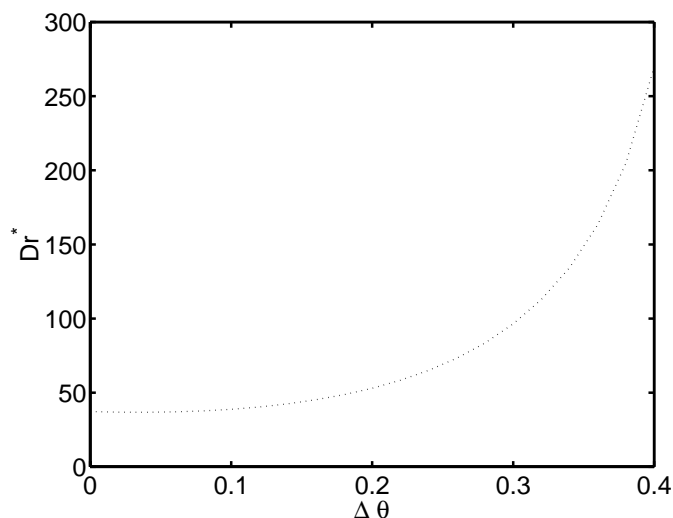


FIG. 11. Critical draw ratio as a function of the nonisothermal parameter $\Delta\theta$. Here all the parameters are the same as in Figure 3.

where $\mathbf{n}_3 = \mathbf{e}_z$; the scalar *uniaxial order parameter* s is related to the polymeric direction \mathbf{m} by

$$(6.2) \quad s = \frac{3}{2} \langle (\mathbf{m} \cdot \mathbf{n}_3)^2 \rangle - \frac{1}{2}, -\frac{1}{2} \leq s \leq 1.$$

The order parameter s describes the average *degree of orientation* between the molecular direction \mathbf{m} and \mathbf{n}_3 . The projection of \mathbf{m} onto the plane orthogonal to \mathbf{n}_3 is isotropic. When $0 < s \leq 1$, the liquid crystal is said to exhibit prolate uniaxial symmetry; when $-1/2 \leq s < 0$, one infers oblate uniaxial symmetry; $s = -1/2$ corresponds to all molecules aligned in the plane orthogonal to \mathbf{n}_3 ; $s = 1$ corresponds to parallel alignment of \mathbf{n}_3 and \mathbf{m} ; finally, $s = 0$ corresponds to an isotropic state.

These relations yield the special uniaxial representation for \mathbf{Q} :

$$(6.3) \quad \mathbf{Q}(z, t) = s(z, t) \operatorname{diag}[-1/3, -1/3, 2/3],$$

where $\operatorname{diag}[-1/3, -1/3, 2/3]$ is a 3×3 diagonal matrix.

Appendix B. Explicit representation of tensor quantities. From (6.3) in Appendix A, one has

$$(6.4) \quad \mathbf{Q} \cdot \mathbf{Q} = s^2 \operatorname{diag}[1/9, 1/9, 4/9],$$

$$(6.5) \quad \mathbf{Q} : \mathbf{Q} = \frac{2}{3} s^2,$$

$$(6.6) \quad \nabla \mathbf{v} : \mathbf{Q} = s v_z,$$

which, together with (2.4), yield

$$(6.7) \quad \hat{\tau} = \text{diag}[\hat{\tau}_{rr}, \hat{\tau}_{\theta\theta}, \hat{\tau}_{zz}],$$

$$(6.8) \quad \hat{\tau}_{rr} = -\eta(\theta)v_z - ck\theta U(s) + 2ck\theta\lambda(\theta)v_z s(1-s),$$

$$(6.9) \quad \hat{\tau}_{\theta\theta} = \hat{\tau}_{rr},$$

$$(6.10) \quad \hat{\tau}_{zz} = 2\eta(\theta)v_z + 2ck\theta U(s) + 2ck\theta\lambda(\theta)v_z s(2s+1).$$

Appendix C. Shape of bulk free energy for variable concentration parameter N . Define

$$(6.11) \quad \begin{aligned} V(s) &= \int U(s) ds = \int s[1 - N/3(1-s)(2s+1)] ds \\ &= \frac{1}{2}s^2 + N/3 \left(\frac{1}{2}s^4 - \frac{1}{3}s^3 - \frac{1}{2}s^2 \right), \end{aligned}$$

where we have imposed $V(0) = 0$. Figure 12 depicts $V(s)$ for different values of N . The important feature is the number of critical points of $V(s)$, i.e., zeroes of $U(s)$, v. N . Note that for low density (e.g., $N = 2$) or higher temperature, only the isotropic equilibrium $s_0 = 0$ exists. As N increases or temperature decreases, the single-well potential for $N < 8/3$ deforms into a double-well potential with isotropic ($s_0 = 0$) and two other equilibria that vary with N .

Appendix D. A simple explanation of the change of velocity profile.

Let us consider the steady state solution of (3.2) in our paper. To show the effect of varying viscosity and also make the analysis as simple as possible (so that we can pinpoint the dominant factor which is most responsible for the phenomenon we have observed), we ignore all other terms except the one involving the viscosity.

The steady state equation simplified as such looks like

$$(6.12) \quad \left(R_{eff}^{-1} \frac{v_z}{v} \right)_z = 0.$$

From (3.3) and (3.4), it is clear that the effective viscosity is roughly of the form

$$(6.13) \quad R_{eff}^{-1} = c_2 e^{c_1/\theta},$$

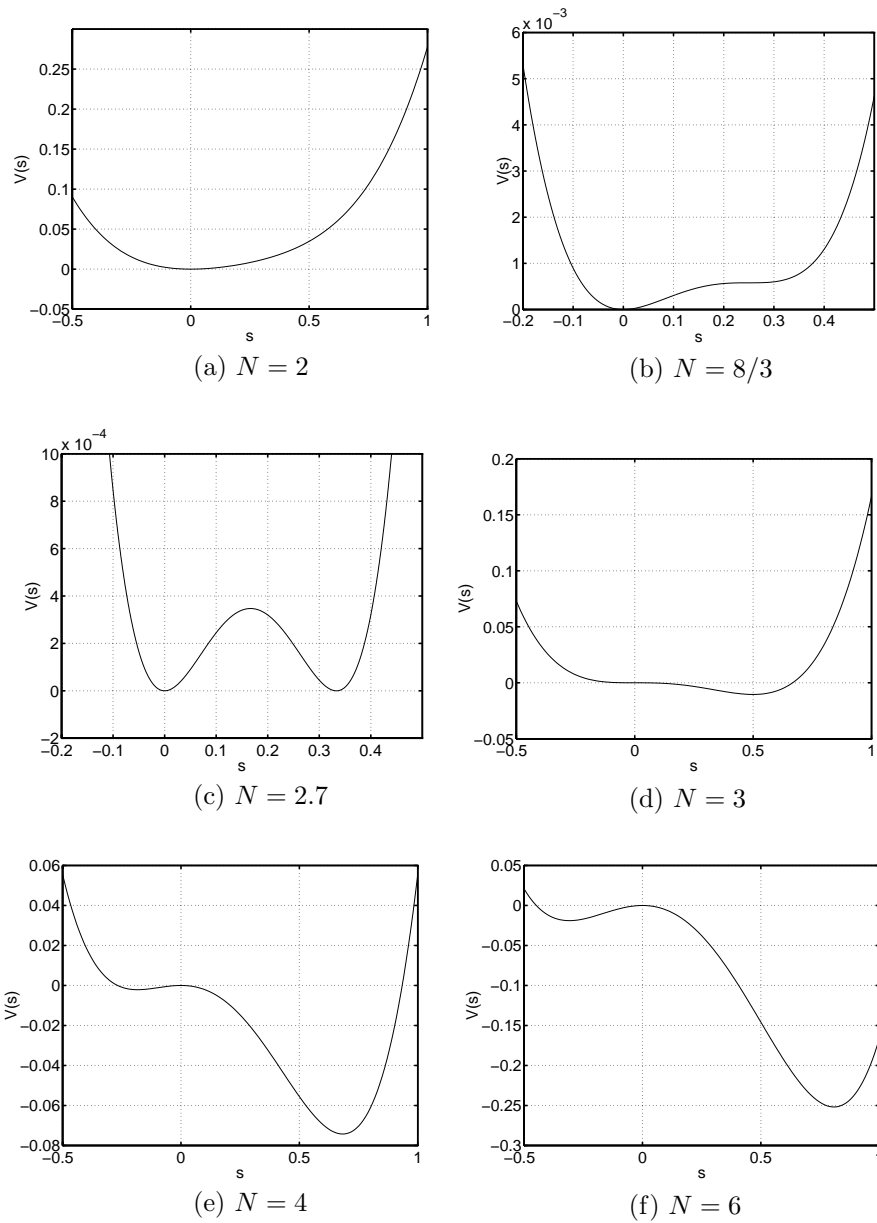
where c_1 is an effective Griffith number.

Since the temperature θ is a decreasing function of z , $1/\theta$ increases with z . A simple increasing function of z is the linear function of the form

$$(6.14) \quad \frac{1}{\theta} = c_3 z + c_4.$$

To make (6.12) easy to solve, we assume that $1/\theta$ is given by (6.14). Substituting (6.14) into (6.13) and renaming the new parameters as c_1 and c_2 , one has

$$(6.15) \quad R_{eff}^{-1} = c_2 e^{c_1 z}.$$

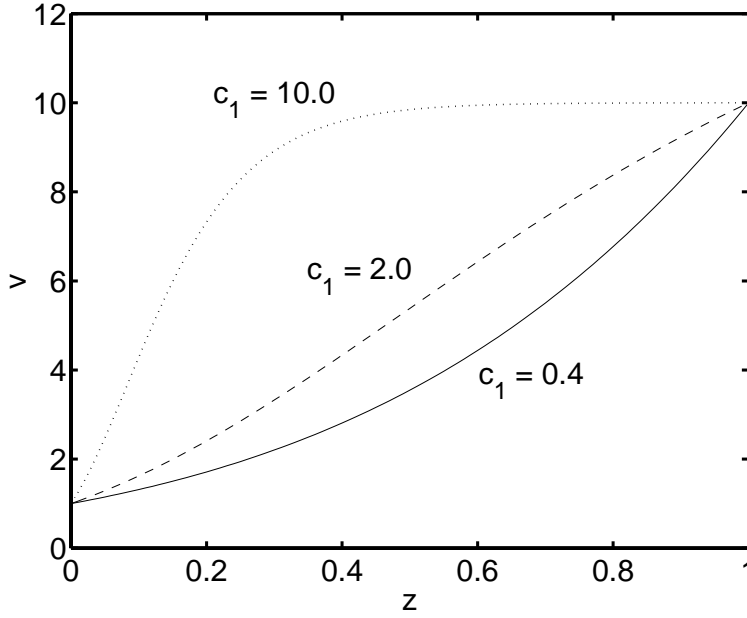
FIG. 12. The 1-D Maier-Saupe excluded-volume potential $V(s)$ for different values of N .

Integrating (6.12) with respect to z yields

$$(6.16) \quad R_{eff}^{-1} \frac{v_z}{v} = c_3,$$

or equivalently,

$$(6.17) \quad (\ln(v))_z = c_2 e^{-c_1 z},$$

FIG. 13. Velocity profiles for different values of c_1 .

where the integration constant c_3 has been absorbed into the parameter c_2 .

Integrating (6.17), one obtains

$$(6.18) \quad \ln(v(z)) = \ln(v(0)) + \left[\frac{c_2(1 - e^{-c_1})}{c_1} \right] \frac{1 - e^{-c_1 z}}{1 - e^{-c_1}}.$$

The boundary conditions

$$(6.19) \quad v(0) = 1,$$

$$(6.20) \quad v(1) = Dr \text{ (draw ratio)}$$

determine the coefficient in brackets in (6.18)

$$(6.21) \quad \left[\frac{c_2(1 - e^{-c_1})}{c_1} \right] = \ln(Dr).$$

Therefore, the solution of (6.12) with boundary conditions (6.19) and (6.20) is

$$(6.22) \quad v(z) = \exp \left[\ln(Dr) \frac{1 - e^{-c_1 z}}{1 - e^{-c_1}} \right].$$

A plot of $v(z)$ for different values of parameter c_1 is shown in Figure 13.

From Figure 13, we make the following observations.

- The velocity profile is concave up for small c_1 and the velocity profile is concave down for large c_1 .

For small c_1 ($c_1 \ll 1$), we have

$$(6.23) \quad \frac{1 - e^{-c_1 z}}{1 - e^{-c_1}} = z + O(c_1)$$

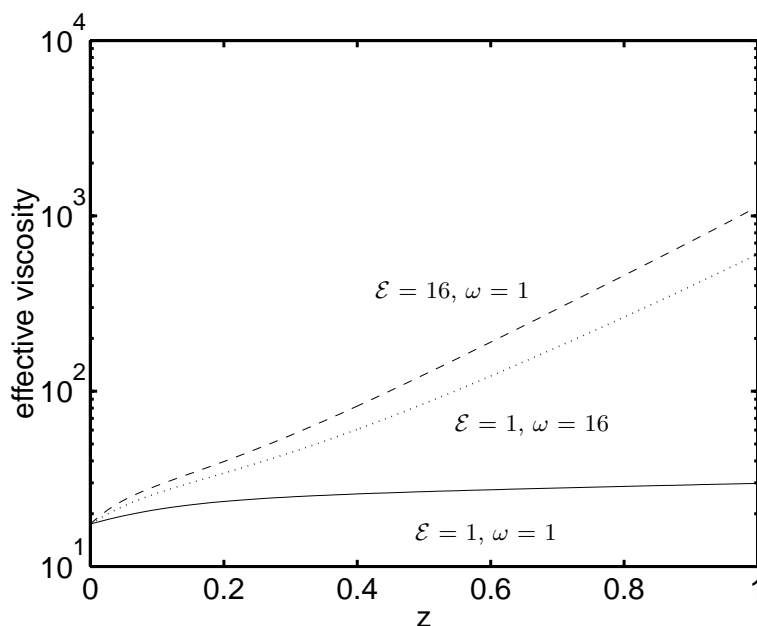


FIG. 14. *Effective viscosity versus z . A logarithmic scale (base 10) is used for the vertical-axis.*

and

$$(6.24) \quad v(z) = \exp[\ln(Dr)z].$$

It is clear that $v(z)$ is concave up for small c_1 .

For large c_1 , $\frac{1-e^{-c_1 z}}{1-e^{-c_1}}$ is a very concave down function.

From the form of R_{eff}^{-1} (see (3.3) and (3.4)), we know that the parameter c_1 is proportional to \mathcal{E} and/or ω . So it is not surprising that the velocity profile is concave down for large \mathcal{E} and/or ω .

- The solution $v(z)$ is independent of the parameter c_2 . The solution of the simplified (6.12) is totally determined by the parameter c_1 . Again from the form of R_{eff}^{-1} , we know that the parameter c_2 is inversely proportional to the Reynolds number. So it not surprising that the velocity profile is virtually unaffected by the Reynolds number.

To verify our assumption in (6.15), in Figure 14 we plot $\log(R_{eff}^{-1})$ as a function of z for various values of \mathcal{E} and ω (based on our numerical simulations). Indeed, $\log(R_{eff}^{-1})$ behaves as a linear function of z , which validates our assumption (6.15).

Acknowledgments. This study is a direct result of long-term collaboration with our colleagues at Hoechst–Celanese Corporation in Charlotte, NC, and Summit, NJ, to whom we are grateful. We further acknowledge a long-term collaboration with Steve Bechtel of Ohio State University on the fundamental foundations of fiber spinning models.

REFERENCES

- [1] D. ACIERNO AND A. A. COLLYER, *Rheology and Processing of Liquid Crystal Polymers*, Chapman and Hall, London, 1996.

- [2] S. E. BECHTEL, K. D. BOLINGER, J. Z. CAO, AND M. G. FOREST, *Torsional effects in high-order viscoelastic thin-filament models*, SIAM J. Appl. Math., 55 (1995), pp. 58–99.
- [3] S. E. BECHTEL, J. Z. CAO, AND M. G. FOREST, *Practical application of a higher order perturbation theory for slender viscoelastic jets and fibers*, J. Non-Newt. Fluid Mech., 41 (1992), pp. 201–273.
- [4] S. E. BECHTEL, M. G. FOREST, D. D. HOLM, AND K. J. LIN, *1-D closure models for 3-D incompressible viscoelastic free jets: von Karman flow geometry and elliptical cross-section*, J. Fluid Mech., 196 (1988), pp. 241–262.
- [5] S. E. BECHTEL, M. G. FOREST, AND K. J. LIN, *Asymptotic 1-D models for 3-D viscoelastic free jets: Closure to all orders*, Stability Appl. Anal. Continua, 2 (1992), pp. 1–43.
- [6] A. V. BHAVE, R. K. MENON, R. C. ARMSTRONG, AND R. A. BROWN, *A constitutive equation for liquid crystalline polymer solutions*, J. Rheology, 37 (1993), pp. 413–441.
- [7] J. A. BURGMAN, *Liquid glass jets in the forming of continuous fibers*, Glass Tech., 11 (1970), pp. 110–116.
- [8] G. CAGINALP, *An analysis of a phase field model of a free boundary*, Arch. Rational Mech. Anal., 92 (1986), pp. 205–245.
- [9] J. R. CASH AND M. H. WRIGHT, *A deferred correction method for nonlinear two-point boundary value problems: Implementation and numerical evaluation*, SIAM J. Sci. Statist. Comput., 12 (1991), pp. 971–989.
- [10] B. F. T. CHUNG AND V. IYER, *Heat transfer from moving fibers in a melt spinning process*, J. Appl. Polym. Sci., 44 (1992), pp. 663–670.
- [11] M. M. DENN, C. J. S. PETRIE, AND P. AVENAS, *Mechanics of steady spinning of a viscoelastic liquid*, AIChE J., 21 (1975), pp. 791–795.
- [12] J. DEWYNNE, J. R. OCKENDON, AND P. WILMOTT, *On a mathematical model for fiber tapering*, SIAM J. Appl. Math., 49 (1989), pp. 983–990.
- [13] M. DOI, *Rheological properties of rodlike polymers in isotropic and liquid crystalline phases*, Ferroelectrics, 30 (1980), pp. 247–254.
- [14] M. DOI, *Molecular dynamics and rheological properties of concentrated solutions of rodlike polymers in isotropic and liquid crystalline phases*, J. Polym. Sci. Polym. Phys. Ed., 19 (1981), pp. 229–243.
- [15] J. L. ERICKSEN, *Liquid crystals with variable degree of orientation*, Arch. Rational Mech. Anal., 113 (1991), pp. 97–120.
- [16] M. DOI AND S. F. EDWARDS, *The Theory of Polymer Dynamics*, Oxford University Press, London, New York, 1986.
- [17] M. G. FOREST AND T. UEDA, *An isothermal model for orientation-induced crystallization in high-speed spinning of liquid crystalline polymer fibers*, J. Non-Newt. Fluid Mech., 84 (1999), pp. 109–121.
- [18] M. G. FOREST AND Q. WANG, *Dynamics of slender viscoelastic free jets*, SIAM J. Appl. Math., 54 (1994), pp. 996–1032.
- [19] M. G. FOREST AND Q. WANG, *The role of microstructure in taming the Rayleigh instability of cylindrical jets*, Phys. D, 123 (1998), pp. 161–182.
- [20] M. G. FOREST, Q. WANG, AND S. E. BECHTEL, *1-D models for thin filaments of liquid crystalline polymers: Coupling of orientation and flow in the stability of simple solutions*, Phys. D, 99 (1997), pp. 527–554.
- [21] M. G. FOREST, Q. WANG, AND S. E. BECHTEL, *1-D isothermal spinning models for liquid crystalline polymer fibers*, J. Rheology, 41 (1997), pp. 821–850.
- [22] M. G. FOREST, H. ZHOU, AND Q. WANG, *A model study of the spinning of thermotropic liquid crystalline polymers: Fiber performance predictions and bounds on throughput*, Adv. Polym. Tech., 18 (1999), pp. 314–335.
- [23] H. H. GEORGE, *Model of steady-state melt spinning at intermediate take-up speeds*, Polym. Engrg. Sci., 22 (1982), pp. 292–299.
- [24] F. T. GEYLING AND G. M. HOMSY, *Extensional instabilities of the glass fiber drawing process*, Glass Tech., 21 (1980), pp. 95–102.
- [25] L. R. GLICKSMAN, *The dynamics of a heated free jet of variable viscosity liquid at low Reynolds numbers*, J. Basic Engrg., September 1968, pp. 343–354.
- [26] G. HENSON, D. CAO, S. E. BECHTEL, AND M. G. FOREST, *A thin-filament melt spinning model with radial resolution of temperature and stress*, J. Rheology, 42 (1998), pp. 329–360.
- [27] B. P. HUYNH AND R. I. TANNER, *Study of the non-isothermal glass fiber drawing process*, Rheology Acta, 22 (1983), pp. 482–499.
- [28] S. KASE AND T. MATSUO, *Studies of melt spinning. I. On the stability of melt spinning*, J. Polym. Sci. A, 3 (1965), pp. 2541–2554.
- [29] J. A. KULKARNI AND A. N. BERIS, *A model for the necking phenomenon in high-speed fiber*

- spinning based on flow-induced crystallization*, J. Rheology, 42 (1998), pp. 971–994.
- [30] M. A. MATOVICH AND J. R. A. PEARSON, *Spinning a molten threadline-steady state isothermal viscous flows*, Ind. Engrg. Chem. Fundam., 8 (1969), pp. 512–520.
 - [31] A. J. MCHUGH, *A continuum model for the dynamics of flow-induced crystallization*, J. Polym. Sci. Polym. Phys. Ed., 34 (1996), pp. 2393–2407.
 - [32] N. MORI, Y. HAMAGUCHI, AND K. NAKAMURA, *Numerical simulation of the spinning flow of liquid crystalline polymers*, J. Rheology, 41 (1997), pp. 1095–1104.
 - [33] S. J. PICKEN, M. G. NORTHOLT, AND S. VAN DER ZWAAG, *Structure and rheology of aramid solutions: Relation to the aramid fiber modulus*, in Processing and Properties of Liquid Crystalline Polymers and LCP-based Blends, D. Acierno and F. La Mantia, eds., ChemTec Publishing, Ontario, Canada, 1993, pp. 1–18.
 - [34] S. RAMALINGAM AND R. C. ARMSTRONG, *Analysis of isothermal spinning of liquid crystalline polymers*, J. Rheology, 37 (1993), pp. 1141–1169.
 - [35] V. V. RAMANAN, V. GAURI, K. W. KOELLING, S. E. BECHTEL, AND M. G. FOREST, *Exploiting accurate spinline measurements for elongational material characterization*, J. Rheology, 41 (1997), pp. 283–306.
 - [36] W. W. SCHULTZ AND S. H. DAVIS, *One-dimensional liquid fibers*, J. Rheology, 26 (1982), pp. 331–345.
 - [37] J. SHIMIZU, N. OKUI, AND T. KIKUTANI, *Simulation of dynamics and structure formation in high-speed melt spinning*, in High-Speed Fibers: Science and Engineering Aspects, Wiley-Interscience, New York, 1985.
 - [38] L. TING AND J. B. KELLER, *Slender jets and thin sheets with surface tension*, SIAM J. Appl. Math., 50 (1990), pp. 1533–1546.
 - [39] G. VASSILATOS, E. R. SCHMELZER, AND M. M. DENN, *Issues concerning the rate of heat transfer from a spinline*, Int. Polymer Proc., 7 (1992), pp. 144–150.
 - [40] Q. WANG, M. G. FOREST, AND S. E. BECHTEL, *1-D models for thin filaments of polymeric liquid crystals*, in Developments in Non-Newtonian Flows, D. A. Siginer and S. E. Bechtel, eds., ASME Press, New York, 1994, pp. 109–118.
 - [41] Q. WANG AND M. G. FOREST, *Numerical simulations of nonisothermal fiber spinning processes*, in Numerical Methods in Non-Newtonian Fluid Dynamics 179, G. C. Vradis and D. A. Siginer, eds., ASME Press, New York, 1994, pp. 11–20.
 - [42] S. L. WANG, R. F. SEKERKA, A. A. WHEELER, B. T. MURRAY, AND S. R. CORIELL, *Thermodynamically-consistent phase-field models for solidification*, Phys. D, 69 (1986), pp. 189–200.
 - [43] Y. WU AND A. KLEINHAMMES, *Private communication*, Department of Physics and Astronomy, University of North Carolina, Chapel Hill, NC; G. COLLINS, *Private communication*, Hoechst–Celanese Corporation.
 - [44] S. ZAHORSKI, *An alternative approach to non-isothermal melt spinning with axial and radial viscosity distributions*, J. Non-Newt. Fluid Mech., 36 (1990), pp. 71–83.
 - [45] A. ZIABICKI, *Fundamentals of Fibre Formation*, John Wiley, New York, 1976.
 - [46] K. F. ZIEMINSKI AND J. E. SPRUIELL, *On-line studies and computer simulation of the melt spinning of Nylon-66 filaments*, J. Appl. Poly. Sci., 35 (1988), pp. 2223–2245.